Helmholtz-Zentrum Dresden-Rossendorf (HZDR)

HELMHOLTZ ZENTRUM
DRESDEN ROSSENDORF

Electron-Beam- and Thermal-Annealing-Induced Structural Transformations in Few-Layer $MnPS_3$

Storm, A.; Köster, J.; Ghorbani Asl, M.; Kretschmer, S.; Gorelik, T. E.; Kinyanjui, M. K.; Krasheninnikov, A.; Kaiser, U.;

Originally published:

February 2023

ACS Nano 17(2023)5, 4250-4260

DOI: https://doi.org/10.1021/acsnano.2c05895

Perma-Link to Publication Repository of HZDR:

https://www.hzdr.de/publications/Publ-36519

Release of the secondary publication
on the basis of the German Copyright Law § 38 Section 4.

Electron-Beam- and Thermal-Annealing-Induced Structural Transformations in Few-Layer $MnPS_3$

Alexander Storm[1#], Janis Köster[1]*, Mahdi Ghorbani-Asl[2], Silvan Kretschmer[2], Tatiana E. Gorelik[1], Michael K. Kinyanjui[1], Arkady V. Krasheninnikov[2,3], and Ute Kaiser[#1]*

[1] Electron Microscopy Group of Materials Science, Ulm University, Albert-Einstein-Allee 11, 89081 Ulm, Germany
[2] Institute of Ion Beam Physics and Materials Research, Helmholtz-Centre Dresden-Rossendorf, 01328 Dresden, Germany
[3]Department of Applied Physics, Aalto University, PO Box 14100, 00076 Aalto, Finland

**These authors contributed equally to this work*
[#]Corresponding Author: Alexander Storm, alexander.storm@uni-ulm.de; Ute Kaiser, ute.kaiser@uni-ulm.de

Abstract

Quasi-two-dimensional (2D) manganese phosphorus trisulfide, $MnPS_3$, which exhibits antiferromagnetic ordering, is a particularly interesting material in the context of magnetism in a system with reduced dimensionality and its potential technological applications. Here, we present an experimental and theoretical study on modifying the properties of freestanding $MnPS_3$ by local structural transformations via electron irradiation in a transmission electron microscope and by thermal annealing in vacuum. In both cases we find that new $MnS_{1-x}P_x$ phases ($0 \leq x < 1$) form in a crystal structure different from the host material, namely that of the α- or γ-MnS type. These phase transformations can be both locally controlled by the size of the electron beam as well as by the total applied electron dose, and simultaneously imaged at the atomic scale. For the MnS structures generated in this process, our ab-initio calculations indicate that their electronic and magnetic properties strongly depend on both in-plane crystallite orientation and thickness. Moreover, the electronic properties of the MnS phases can be further tuned by alloying with phosphorus, suggesting a novel route toward the design of lateral heterostructures. Therefore, our results may enable pathways for the controlled growth of new phases with distinct properties embedded in freestanding quasi-2D $MnPS_3$.

Keywords

Structural transformations, $MnPS_3$, α-MnS, γ-MnS, 3D electron diffraction, thermal annealing, modification,

The ability to characterize and modify materials at the atomic scale is as important for the progress in nanotechnology[1,2] as the precise control over their growth. To this purpose, aberration-corrected (AC) high-resolution (HR) *in situ* transmission electron microscopy (TEM)[3,4], along with scanning transmission electron microscopy (STEM)[5,6], as well as scanning tunneling microscopy (STM)[7,8] is one of the indispensable techniques that provides information about the atomic structure of the specimen and its transformations in real-time[9–11].

On the other hand, with the help of (S)TEM techniques, depending on the choice of the size of the electron beam, structural modifications can be introduced locally down to the atomic level[12] as result

of the interaction of the highly accelerated electrons with the specimen[5,13–15]. The modification of ultrathin nanolayers has recently attracted considerable attention, as the structure and, thus, properties of two-dimensional (2D) materials can be altered more easily (as compared to bulk systems) due to their geometry. Specifically, the crystallographic, electronic, and magnetic properties of 2D materials can be tuned by creating single-[16–18] and extended defects[19–21] as well as by the adsorption of atoms[22,23]. Moreover, (S)TEM can be used to cause spatially-localized phase transformations in crystalline few-layer or monolayer materials and, therefore, significantly alter their local properties. (S)TEM studies of various low-dimensional materials have been carried out. Controllable structural transformations in transition metal dichalcogenides (TMDs)[18,24–26], alumina[27], silica[28], and nanowires[29,30] have been reported, as well as the formation of Pb nanoparticles on $CsPbX_3$ nanocrystals[31], just to mention a few. Further, phase transformations in two-dimensional materials induced by STM are reported[11,32,33]. The advantage of electron-beam-mediated modification compared to other conventional processes (e.g., heating[34], electrostatic gating[35], strain engineering[36–38]) to induce 2D phase transformations is the control over the transformation process down to the atomic scale in real-time[25,29]. Thus, (S)TEM is next to STM a paramount tool for locally engineering the properties of 2D materials.

Within the class of 2D materials, the spotlight has recently turned to transition metal phosphorous trisulfides (TMPTs). Among them, manganese phosphorous trisulfide ($MnPS_3$) has received the most attention. $MnPS_3$ crystallizes in the monoclinic space group C2/m[39], in which magnetic Mn^{2+} ions are octahedrally coordinated to six S atoms with a dumbbell-shape structure $[P_2S_6]^{4-}$, occupied by P-P groups in the centers of the hexagons[40–42]. $MnPS_3$ has inherent magnetic properties[43,44], persisting even when the material is thinned down to few-layers[45], with a bandgap of about 3 eV[46], making it an ideal candidate for multifunctional electronics/spintronics[47–49] and battery[50] applications. Moreover, it has been shown that the intrinsic properties of $MnPS_3$ can be significantly tailored. For instance, pressure-driven compression has proven to significantly modify the magnetic properties as well as to force an insulator-metal transition[51–53]. In addition, a reduction of intralayer coupling and a change of the magnetic properties of few-layer $MnPS_3$ occur upon suitable intercalations[54–56]. Moreover, it has already been shown that MnS type systems are promising candidates for various applications. For instance, α-MnS was proposed as a new promising anode material for post-lithium batteries[57–59] and an interesting candidate for future electronic devices, e.g., in field-effects transistors[60]. Our recent TEM study already showed that few-layer TMPTs lose predominantly sulfur as a result of their interaction with the impinging electrons, which in turn leads to strong modifications of the pristine material[61].

However, the change in properties of free-standing few-layer $MnPS_3$/MnS systems due to electron-beam-induced phase transformations and due to annealing has not been investigated so far in detail.

Here, we investigate in detail the effects of electron irradiation and annealing on few-layer $MnPS_3$. We find phase transformations and identify their crystallographic and electronic structures using a combination of chromatic and spherical aberration (Cc/Cs)-corrected -80kV HRTEM, 3D electron diffraction (3D ED), electron energy loss spectroscopy (EELS), and energy-dispersive X-ray spectroscopy (EDX). First, we show that electron irradiation primarily leads to the growth of one distinct new $MnS_{1-x}P_x$ phase (α-MnS type, $0 \leq x < 1$) oriented in a defined manner within the host $MnPS_3$. This phase transformation of $MnPS_3$ can be locally controlled by tuning the size of the electron beam down to a nanometer scale. Further, we show that the area of the emerging phase can be tuned by the total applied electron dose. After the complete degradation of the host other orientations of the ultrathin $MnS_{1-x}P_x$ phases also in the γ-MnS type are emerging. High stability of the observed freestanding phases under the electron beam and under even ambient atmosphere was found, which is confirmed by ab-initio calculations for different P concentrations down to the monolayer limit, yet the experimental findings indicate a high S and a low P concentration. Second, annealing in vacuum was used to transform few-layer $MnPS_3$ into pure α-MnS and we found a phase transition temperature of 490°C. By density functional theory calculations, we show that the electronic and magnetic properties of the formed MnS type phases strongly depend on thickness and their in-plane orientation. The electronic properties of MnS type phases can be further tuned by alloying with phosphorus. As a result, our results indicate new pathways of the controlled growth of unique phases with various properties starting from few-layer $MnPS_3$.

Results and Discussion

Phase transformation in few-layer $MnPS_3$ observed under the electron beam in the TEM

In Figure 1 (a.1-a.3), we present an 80 kV Cc/Cs-corrected HRTEM image sequence illustrating the evolution of few-layer $MnPS_3$ under the electron beam with a constant dose rate of $0.5 \times 10^6 \frac{e^-}{s\,nm^2}$. Figure 1 (a.1) shows the pristine material, viewed along the normal incidence direction [103] (see Figure S1) of $MnPS_3$, where a magnified region is depicted on the right-hand side. After irradiation, in Figure 1 (a.2, a.3), changes in the material are evident: islands with an altered structure continuously grow within the parent matrix. The projected areas of the newly emerging structure are clearly observable also in the FFT-mask filtered images presented next to the HRTEM images (dyed areas). The projected areas are generated by selecting the reflections of the new phase in the FFT of the corresponding images, and the applied filter mask is presented in Figure S2. From these projected areas, the proportion of the new structure to the total imaged area is quantified and compared with the total accumulated dose in Figure 1 (b); a linear dependence can be inferred.

As shown in our previous study, a primary removal of sulfur (S) and phosphorus (P) atoms by 80 keV electrons is favored via direct electron-nucleus collision[61]. This leads to an S deficiency in electron

beam exposed regions of few-layer $MnPS_3$ (see Figure S3) and, therefore, can lead to the growth of new structures.

Extensive studies (TEM experiments and computational calculations) with a wide variety of materials have shown that atoms in layers facing the electron beam are considerably lower affected than the beam exit surface (here the bottom layer) by electron beam-sputtering via direct electron-nucleus collisions[62–64]. This can be attributed to the elastic interaction of the electron beam with the target atoms and following momentum transfer considerations of these elastic processes, see e.g.[64]. Especially considering a single-layer, the displacement thresholds for chalcogen atoms facing the beam (in the top chalcogen layer) proved to be higher than for the bottom chalcogen layer[10,65,66]. Assuming that additional layers are present on a single-layer (few-layer), it can be assumed that the outer layers of the few-layer system are influenced primarily by the electron beam (or most likely the bottom layer first, see inset in Figure 1 (b)). To facilitate the supposed transformation process in $MnPS_3$, an experimental and two corresponding FFT-mask filtered images are depicted in Figure 1 (c). If the $MnPS_3$ atomic lattice is FFT-mask filtered, the structure extends over the entire sample area. In contrast, the new structure is only present in the red-framed areas. This indicates that the new phase spreads primarily laterally (in-plane), while intact $MnPS_3$ layers are present on top or underneath. A modeled bi-layer scheme beneath visualizes the occurring new structure (red) embedded in an isolated $MnPS_3$ layer (gray). While the 1st layer is hardly affected by the electron beam remaining virtually intact, new structures emerge in the 2nd layer due to the removal of S and P atoms. Therefore, we propose that in $MnPS_3$, a new structure grows primarily within one layer after the other in the few-layer host, and the transformation starts first at the bottom layer.

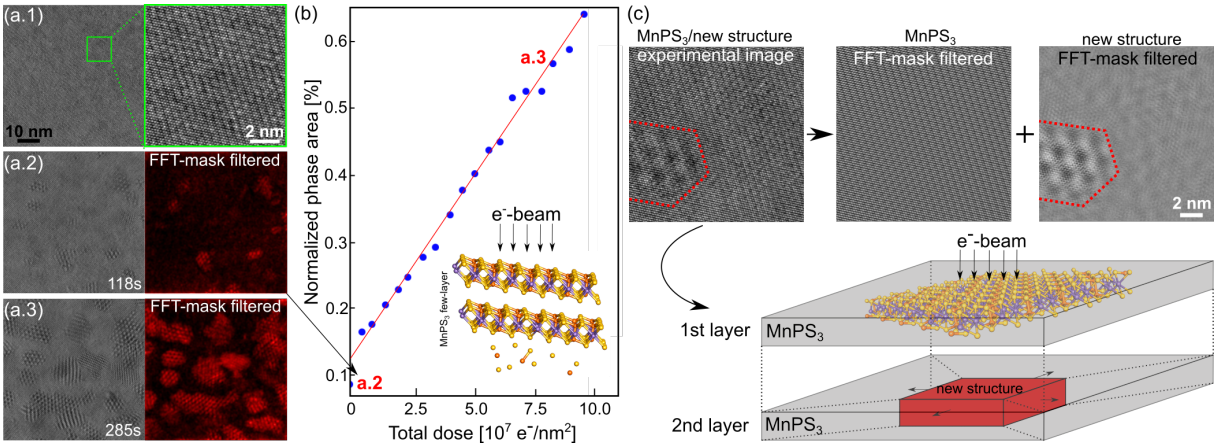

Figure 1. Panels (a.1-a.3) show 80 kV Cc/Cs-corrected HRTEM images of $MnPS_3$ acquired under a dose rate of $0.5 \times 10^6 \frac{e^-}{s\,nm^2}$. (a.1) Pristine $MnPS_3$ structure. (a.2, a.3) Irradiated and FFT-mask filtered images with phase-islands highlighted in red. The normalized measured area of the newly grown phase is shown in the diagram in panel (b). A linear increase with accumulated dose can be inferred. The points corresponding to the structures shown in panel (a) are marked. (c) An experimental and corresponding FFT-mask filtered images ($MnPS_3$ and new phase) are shown. The applied filter mask

(FFT) is shown in Figure S2. Schematic illustration of the structure of the newly formed and embedded phase in an isolated $MnPS_3$ layer (2nd layer) is shown beneath.

3D ED was used to determine the lattice parameters (unit cell) of the newly formed phases[67]. Few-layer $MnPS_3$ was irradiated until additional Bragg reflections of the new phases were clearly seen in ED data (see Figure 2 (a,b)). Two distinct new phases (labeled as phases 1 and 2) can be detected; reflections corresponding to phase 1 have higher intensities and match the observed embedded phase of Figure 1. The irradiated crystal was tilted in the TEM within ±60° with a tilt increment of 1°. At each tilt position of the crystal, a diffraction pattern was collected. A tilt series of the patterns was reconstructed into a 3D reciprocal space (exemplary diffraction patterns are presented in Figure S4 (a)). The diffraction volume[67] in Figure 2 (c) exhibits an overlay of two pronounced crystalline lattices - the $MnPS_3$ host (blue) and the new phase 1 (red).

The extracted positions of the red reflections align well with a single lattice suggesting that all inclusions have a similar orientation within the matrix. This new lattice was found to be cubic with the unit cell parameters: a=2.47 Å, b=2.56 Å, c=2.67 Å, α=90.1° β=89.4°, and γ=90.3°, and the lattice parameters of the new cubic unit cell corresponding to the Mn-S bond length in $MnPS_3$ of 2.61 Å. More details about the reconstruction of the reciprocal space and the assignment of the crystal lattices can be found in the SI section 2.

Therefore, 3D ED indicates that phase 1 is a NaCl type F-centered lattice with a cell parameter of 5.21 Å. The most stable compound in the Mn-P-S system with the NaCl structure type is the mineral Alabandite – α-MnS with the lattice constant of 5.22 Å[68], space group Fm-3m, with Mn being bi-valent. The elemental composition of the present phase could be different from the strict MnS stoichiometry; therefore, we assign phase 1 to α-MnS_xP_{1-x}, see Figure 2 (d). The peak at 1.84 Å of Figure 2 (b) can then be attributed to the 002 α-MnS_xP_{1-x} reflection, and the lattice of phase 1 is aligned with the [111] direction, see Figure 2 (d), along the [103] of the host $MnPS_3$. Further, these are the identical orientations as observed in HRTEM experiments presented in Figure 1.

Unambiguous identification of phase 2 by 3D ED was not possible due to the weak reflections. Nevertheless, in combination with HRTEM, phase 2 is identified, elaborated in detail below.

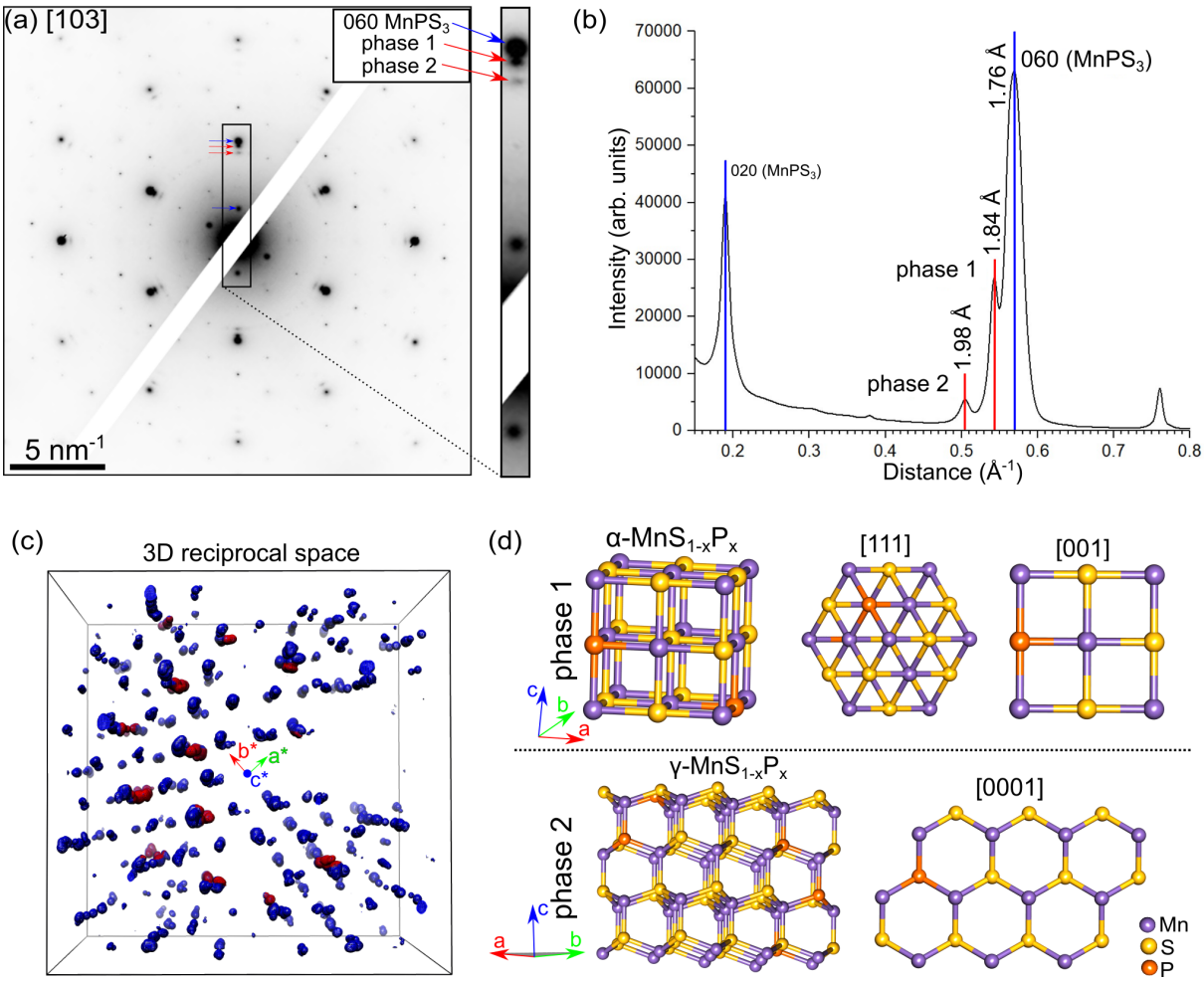

Figure 2. (a) Normal incidence [103] diffraction pattern of $MnPS_3$ after pre-irradiation with 80 keV electrons. Next to the spots of the host material $MnPS_3$, diffraction spots of two new emerging phases (phase 1 and phase 2) can be observed. (b) A line profile of the diffraction pattern in (a) along the highlighted direction is shown, and the observed peaks of the different phases are marked accordingly. (c) Reconstructed 3D ED reciprocal space of the irradiated crystal. The parent $MnPS_3$ phase (blue) and the new phase (red) are segmented. (d) Structure models of the new emerging phases α-$MnS_{1-x}P_x$ (phase 1) and γ-$MnS_{1-x}P_x$ (phase 2) are presented. The orientation of the shown structure models illustrates the primarily observed orientations of the new phases aligned to the host $MnPS_3$.

From 3D ED, it is not feasible to determine the exact S:P ratio of α-MnS_xP_{1-x} and to find out whether the Mn valence is bi-valent (2+) in the new cubic phase 1. However, a detailed spatially resolved EELS analysis (Figure S5) indicates that predominantly S can be measured and that the Mn valence state is predominantly 2+. Therefore, our combined experiments are evidence of the formation of Mn(II, III)$S_{1-x}P_x$ with the NaCl structure (α-$MnS_{1-x}P_x$), and the lattice parameter of 5.21 Å, Figure 2 (d), with high S and low P concentration.

The experiments indicate that at the beginning of the irradiation process, the electron beam causes the transformation of the host material to the cubic α-$MnS_{1-x}P_x$ aligned with [111] direction parallel to the normal incidence [103] of the $MnPS_3$ host matrix. With increasing imaging time (i.e., larger total

accumulated dose), freestanding patches of the newly formed phases could be imaged after the host has be completely degraded. An experimental HRTEM image of a newly grown isolated α-$MnS_{1-x}P_x$ crystal is presented in Figure 3 (a). A magnified part of the image is shown in the red frame. An overlay of the simulated image with the atomic model of the cubic α-$MnS_{1-x}P_x$ phase, oriented along the [111] direction, highlights the atomic column contrast. The lattice parameters match the found α-$MnS_{1-x}P_x$ phase in the 3D ED, see Figure 2. At this transformation stage, different orientations of the α-$MnS_{1-x}P_x$ emerge and can be imaged as freestanding structures as well. Figure 3 (b) shows the HRTEM image of an α-$MnS_{1-x}P_x$ patch viewed along the [001] direction, with a magnified part shown in the green framed area. The experimental image agrees well with the simulated HRTEM image for this orientation. Additional HRTEM images of the $MnS_{1-x}P_x$ crystals are provided in Figure S6.

The analysis of the normal incidence ED pattern in Figure 2 (a,b) revealed an additional set of weak diffraction spots aligned with the two other lattices ($MnPS_3$ and cubic α-$MnS_{1-x}P_x$) belonging to the unidentified phase 2. These reflections appeared at later stages of the structural transformation, and the reflections appeared as small arks; sometimes, parts of diffraction rings were seen. We attribute this to a partial loss of the orientation relationship of phase 2 to the host $MnPS_3$. The search for a suitable phase candidate resulted in the hexagonal γ-$MnS_{1-x}P_x$, see Figure 2 (d), with the wurtzite structure[69]. The structural characterization of this phase was complicated by the presence of the two other phases. Yet, the reflection positions match the observed data well. For example, the peak at 1.98 Å (in Figure 2 (b)) matches the $2\bar{1}\bar{1}0$ γ-$MnS_{1-x}P_x$ reflection. In addition, ultrathin patches of phase 2 could also be found in experimental HRTEM images at the later transformation stage. Figure 3 (c) shows a patch of the γ-$MnS_{1-x}P_x$ in the [0001] direction, a magnified image of this area is shown in blue. The observed contrast agrees well with corresponding image simulations of γ-$MnS_{1-x}P_x$ [0001]. Further examples of HRTEM images of different crystallographic orientations of γ-$MnS_{1-x}P_x$ are presented in Figure S6 (e).

The energetics of emerging α-$MnS_{1-x}P_x$ and γ-$MnS_{1-x}P_x$ phases at room temperature were studied using first-principles calculations. To analyze the stability of such compounds, the convex hull was constructed (see Figure S7) based on the formation enthalpy per atom

$$H_{Form}(MnS_{1-x}P_x) = [E(MnS_{1-x}P_x) - xE(MnS) - (1-x)E(MnP)]/2,$$

where x denotes the phosphorus concentration and $E(MnS_{1-x}P_x)$, E(MnS), E(MnP) are the energies of the mixed compound and the pure phases as obtained by DFT calculations, respectively. Using a convex hull is a standard approach in materials science to assess the relative stability of materials with different stoichiometries. More details about the stability calculations can be found in the SI section 4. In the case of α-[111] $MnS_{1-x}P_x$, several mixed compounds (e.g., for x=0, 0.625, 1) are on the convex hull, suggesting that these materials should be at least metastable. As for other unstable compounds,

the energy differences to the convex hull are in the meV range, such that at room temperature, the mixing entropy[70] per atom

$$S_{mix}(x) = - [x\ln(x) + (1-x)\ln(1-x)]k_B/2$$

may stabilize the compounds, see Figure 3, where the Gibbs free energy difference $\Delta G = \Delta H - Ts_{mix}$ to the convex hull is plotted on the right-hand side. Compared to the [111] direction, the $MnS_{1-x}P_x$ sheets with the surface oriented in [001] direction show higher stability at a wide range of low P concentrations. In the case of γ phase, the stabilization of the mixed $MnS_{1-x}P_x$ compound in [0001] direction requires a higher fraction of phosphorus as compared to the α -phase.

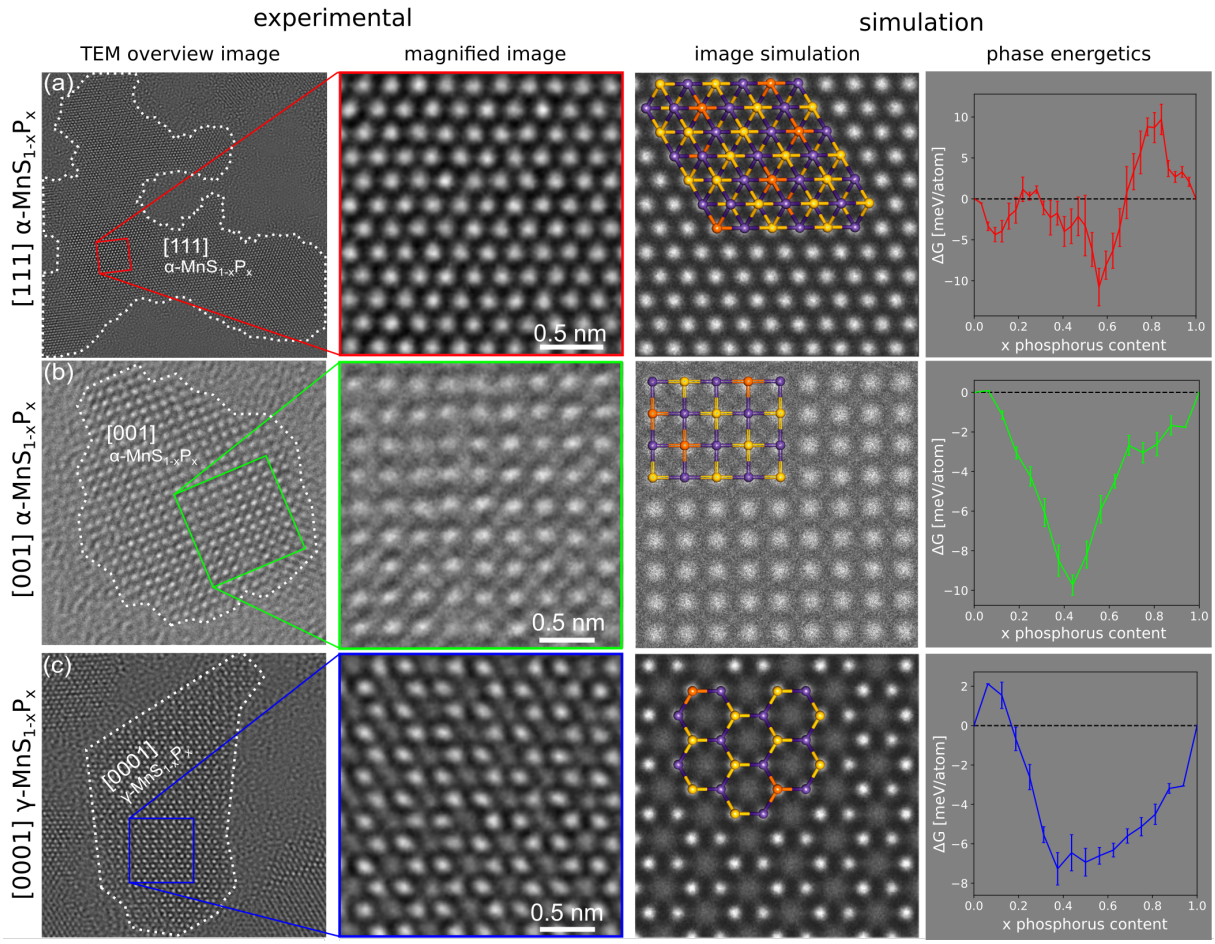

Figure 3. 80 kV Cc/Cs-corrected HRTEM images of $MnS_{1-x}P_x$ crystals and the energetics of the phases. (a) α-$MnS_{1-x}P_x$ in [111] direction, (b) α-$MnS_{1-x}P_x$ in [001] direction, and (c) γ-$MnS_{1-x}P_x$ in [0001] direction is shown. Magnified regions are marked and presented beside. In addition, the experimental images are complemented by HRTEM image simulations. The calculated convex hulls are shown in the right panels.

Phase transformation in few-layer $MnPS_3$ caused by annealing and analyzed in TEM

Phase transformations caused by electron beam irradiation were studied in the previous section in detail, and here structural modifications caused by *in situ* annealing of the sample are analyzed to gain further insight into structural changes in $MnPS_3$.

Pristine $MnPS_3$ flakes of different thicknesses were heated *in situ* stepwise (~ 10°C) (technical details are given in **Materials and Instrumentations)**, and structure transformations were observed at 490°C, see Figure S8. The sample appeared completely different after the annealing experiments. No large $MnPS_3$ flakes were observed, but instead, clustered polycrystalline nanocrystals emerged. The morphology change indicates a complete structure transformation of $MnPS_3$.

To analyze the elemental composition of the annealed structure, STEM-HAADF images and EDX elemental maps (80 kV) were acquired on different sample positions, Figure 4 (a), which were annealed at a temperature of 600°C. The HAADF images show the altered structure, and the elemental maps of Mn and S prove the presence of these elements. In Figure 4 (b), a detailed EDX spectrum of the annealed sample is given, and the observed peaks are labeled to the corresponding element edges. In addition, the corresponding atomic fractions and errors are presented in Figure 4 (b) as a table. Mainly, Mn and S can be observed, as well as small amounts of C, O, and residual P. These results indicate that additional carbon contamination is present (discussed in more detail in SI section 5, see also Figure S9) and residual oxidized Mn, P, and S. From the elemental analysis, the main structure is expected to consist of Mn and S atoms.

To determine the valence, core-loss EELS of the Mn-$L_{2,3}$ edge is performed and presented in Figure 4 (c). The white line ratio[71] of the L_3 to the L_2 gives a value of 4.50, which suggests that the structure mainly contains Mn (2+)[61,71].

Selected area electron diffraction experiments were performed on the annealed sample as well (see Figure S10 (a)), and an azimuthally integrated (elliptical distortion corrected) pattern is shown in Figure 4 (d). A simulated powder diffraction pattern of alabandite - F-centered cubic $Mn^{2+}S^{2-}$ is shown in red. The simulated and experimental patterns are in good agreement, indicating the formation of alabandite due to the annealing of pristine $MnPS_3$. An additional peak at 0.45 $Å^{-1}$ corresponds to 2.2 Å and is likely associated with graphitic contaminations formed at the surface (the presence of carbon is found in the EDX elemental quantification as well, see Table in Figure 4 (b)).

To verify the formation of alabandite, the annealed structure was imaged in Cc/Cs-corrected HRTEM at 80kV. In Figure 4 (e), a typical crystalline grain is shown, and its magnified region is presented in Figure 4 (f). A cubic lattice oriented along [100] direction can clearly be identified. The distances in x- and y- directions between atomic columns in Figure 4 (f) are 2.60 Å and 2.58 Å, respectively, fitting well with the expected values of 2.62 Å[68] for the alabandite structure projected in [100]. The FFT of the image in Figure 4 (e) is shown in Figure 4 (g), and the measured reciprocal distances

($0.38\ \text{Å}^{-1}$, $0.54\ \text{Å}^{-1}$, $0.77\ \text{Å}^{-1}$) of the observed reflections are in good agreement with the azimuthally integrated distances shown in Figure 4 (d).

Core-loss EELS spectra of the annealed sample show that next to the pristine alabandite, oxidized phosphorus is formed, see Figure S10. Therefore, we conclude that during the annealing process, $MnPS_3$ is transformed to alabandite with the formation of graphitic contamination at the surface and oxidized residuals. When the sample is annealed to higher temperatures, the observed polycrystalline clusters reassemble into larger alabandite nanocrystals, which are also stable, as evident from Figure S11.

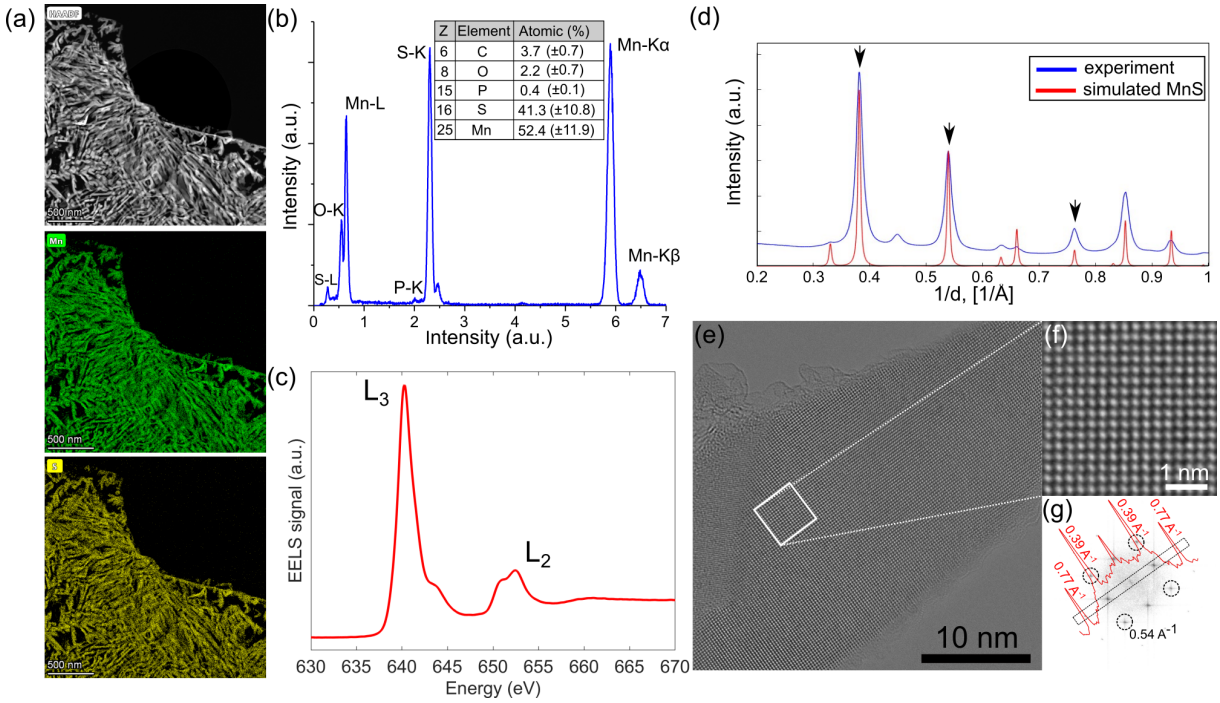

Figure 4. Analytical TEM of annealed $MnPS_3$ (for 40 min at 600 °C). (a) HAADF and corresponding EDX Mn and S elemental maps of the structure obtained after annealing. (b) EDX spectrum of a freestanding annealed sample and the observed peaks are labeled with the corresponding elemental transitions. In addition, an elemental quantification is presented, and mainly S and Mn can be found. (c) Core-loss EELS of the Mn $L_{2,3}$ –edge of the heated sample is given. (d) Scattering profile of a diffraction pattern of MnS powder. The experimental curve (blue) is divided by d (interplanar distance) to enhance the intensities at higher scattering angles. The red curve corresponds to simulated MnS. An 80 kV Cc/Cs-corrected HRTEM image in (e) shows a crystalline grain of the polycrystalline MnS structure. (f) Aligned magnified region of the structure presented in panel (e). The corresponding FFT of that structure is shown in (g); the red curve illustrates a line scan along the black dotted box in (g).

We further studied the electronic and magnetic properties of new MnS polymorphs using DFT calculations. The energetically favored magnetic ordering was determined for monolayer and bilayer systems, see Figure S12. The stability of facets was studied for both the ferromagnetic (FM) and antiferromagnetic (AFM) alignments of the spins in Mn layers. In the case of the α-MnS phase, the [001] facet is more stable in the AFM state than in the FM state, whereas [111] facet prefers to remain

in the FM state. In the case of the γ-MnS phase, however, the thickness of the slab influences the magnetic character of the system, changing the ordering from ferromagnetic to antiferromagnetic. Our results show that the electronic structure of bulk MnS is significantly modified in the new polymorphs. For the bulk material, DFT+U calculations yield a band gap of 1.43 eV originating from a transition between the valence band maxima (VBM) situated at the *M* point and the conduction band minima (CBM) at the Γ point, see Figure S13 and Table S1. In the case of the slabs, the material can be either semiconducting or metallic, depending on the orientation and the thickness of the facets. In the MnS monolayer limit, α-[001] and γ-[0001] phases are semiconductors with band gaps of 0.03 and 0.23 eV, while the α-[111] monolayer has a metallic character. As PBE generally underestimates electronic band gaps, as discussed in the literature, see, e.g[72] and references therein, we further calculated the band gaps using more advanced approaches such as DFT+U, and Heyd-Scuseria-Ernzerhof (HSE) hybrid functional (Table 1). Note that we list the calculated PBE gaps for the reference only. More technical details regarding the ab-initio calculations are given in the **Materials and Instrumentation** section. The DFT+U calculations using onsite *U* values on transition metal atoms increase the magnitude of the band gap to 0.83 and 1.98 eV for α-[001] MnS and γ-[0001] MnS monolayer, respectively. Similarly, the band gap values at HSE levels increase to 0.66 (2.34) for α (γ) type phases, respectively. The electronic band structures indicate that the band gap in α-[001] MnS monolayer from an indirect transition from the VBM at the *X* point to the CBM at the Γ point, Figure 5. In contrast, the monolayer in the γ-[0001] MnS phase has a direct band gap at the Γ point. Furthermore, the electronic structure of the γ-MnS phase shows a strong dependence on the thickness of the facets. If the thickness of the [001] slab increases from mono to bilayer, the size of the band gap decreases, which is accompanied by a direct to indirect gap transition, Figure 5. In the case of α-[001] MnS phase, however, the electronic structure remains almost intact by increasing the thickness from monolayer to bilayer. We also note that the magnetic moments and phase ordering do not depend on the degree of localization of the exchange-correlation as shown previously[73].

Table 1. The Band Gap Values (eV) of MnS Polytypes Calculated at Different Levels of Theory.

MnS polytypes	DFT+PBE	DFT+U	DFT+HSE
α-[001] 1L/2L	0.03/0.02	0.83/0.83	0.66/0.66
γ-[0001] 1L/2L	0.23/0.03	1.98/1.68	2.34/2.04

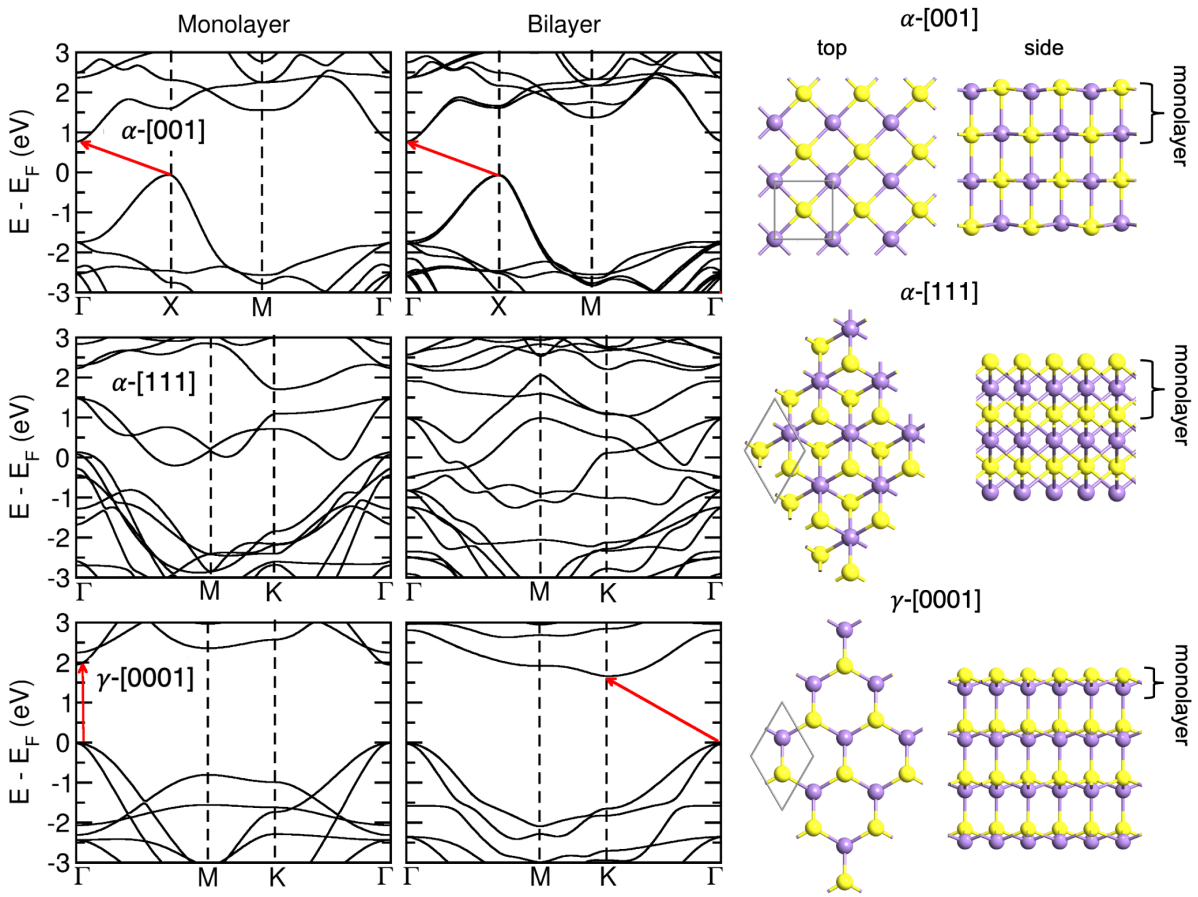

Figure 5. Electronic band structure of various MnS monolayer and bilayer polytypes. The calculations are performed using the DFT+U method. Optimized atomistic structures are shown on the right in the top and side views. The atomic structure of the monolayer is indicated. Yellow and lilac balls represent S and Mn atoms, respectively. The energetically preferred magnetic ordering is presented in Figure S12.

To get more insights into the effects of phosphorus alloying on the electronic properties of MnS, the electronic structures of the mixed compounds were investigated. Only γ-[0001] type monolayer was considered, as it possesses a relatively large band gap. Figure 6 shows the projected electron density of states for pristine MnS and alloyed $MnS_{1-x}P_x$ monolayer. After introducing P into the MnS system, the new occupied electronic states appear at the valence-band edge making the mixed compound metallic at higher P concentration. Since P has one electron less as compared to S and can be referred to as an acceptor dopant, it shifts the Fermi level to the valence band. In the case of 6% P concentration ($MnS_{0.94}P_{0.06}$), the defect-induced states show small dispersion formed from the *p* atomic orbitals of phosphorus atoms. The electron density plot also indicates highly localized states on the P atom with some smaller contributions from the next adjacent Mn atoms (see Figure 6 (b)). By increasing the P concentration to 25%, the midgap states are more delocalized around the Fermi level.

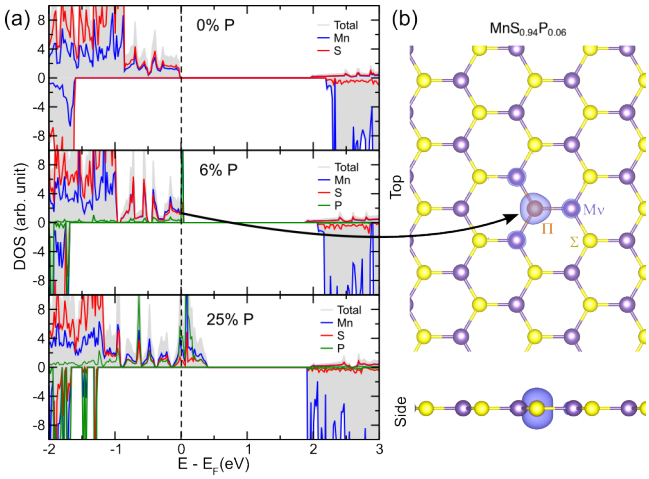

Figure 6. (a) The projected density of states of γ -[0001] $MnS_{1-x}P_x$ monolayer with the spin-up and spin-down components corresponding to positive and negative values. The Fermi level is shifted to zero. The P-associated states are clearly seen at the edge of the valence band. (b) The partial charge densities at the Fermi level for $MnS_{0.94}P_{0.06}$ monolayer. The isosurface value is set to 0.001 eÅ^{-3}.

Conclusion

Our *in-situ* Cc/Cs-corrected HRTEM experiments provided insights into the annealing and electron-beam-induced structure transformations of $MnPS_3$. We showed that suitable dose rates allow for a controlled growth of α-MnS type phases embedded in the host system, with the crystals being oriented with their [111] direction along the c* direction of the parent $MnPS_3$. In addition, we predict that the discovered α-MnS type phases are alloyed with P forming α-$MnS_{1-x}P_x$ structures. At later stages of irradiation, different orientations of α-$MnS_{1-x}P_x$ and a new phase γ-$MnS_{1-x}P_x$ emerge, and the stability of all observed phases is confirmed by ab-initio calculations.

Another route to transform $MnPS_3$ into pure α-MnS was proven to be in situ annealing under vacuum conditions. This finding indicates that there exist different pathways to a controlled nanoscale transformation of a few-layer antiferromagnetic host into other stable phases, even down to ultrathin films. However, in the case of annealing, the complete sample is transformed to MnS, whereas in the electron beam irradiation case, the process can be controlled by the size of the electron beam and the total applied electron dose.

Our DFT calculations reveal that the pure MnS phases can show diverse magnetic and electronic properties depending on the orientation and thickness of the facets. In particular, α-[001] MnS monolayer is an antiferromagnetic semiconductor with an indirect band gap, while γ-[0001] MnS monolayer was found to be a ferromagnetic semiconductor with a direct band gap. We further showed that the confinement effects in γ-[0001] MnS facets are strong, giving rise to a direct to indirect band gap transition. In addition, alloying with phosphorus (i.e. $MnS_{1-x}P_x$, $0 \leq x < 1$) was found to be a

powerful technique to tailor the electronic and optical properties of the MnS facets. Further, we provide evidence that the mixed $MnS_{1-x}P_x$ phases in both α- and γ- type can be stable for certain phosphorus concentrations. We conclude that if the thickness and orientation of the $MnS_{1-x}P_x$ phases can be controlled appropriately, such compounds have great potential as novel 2D materials for various optoelectronic applications. For instance, one future pathway might be to partially irradiate a few-layer $MnPS_3$ flake to create a $MnPS_3$/ $MnS_{1-x}P_x$ lateral heterostructure with varying properties depending on the flake thickness and lateral extent of the interface.

Materials and Instrumentations

Materials: Thin flakes of TMPTs were prepared by a polymer-assisted sample preparation method based on mechanical exfoliation. Bulk crystals were thinned down by exfoliation via an adhesive tape and pressed on a PVA coated Si substrate. The underlying polymer layer allows a gentle transfer with distilled water of the thin flakes to a Quantifoil grid[74].

Specimens for annealing are prepared by stamping a PMMA layer onto a *ThermoFisher* micro-electro-mechanical system (MEMS)-chip (note: isopropyl alcohol can be helpful to bring the PMMA layer in contact with the chip surface). Finally, the chip is dipped first into acetone and then in distilled water to remove PMMA residuals.

Characterization and equipment: HRTEM experiments were conducted with a Cs-corrected TEM FEI Titan 80 – 300 and the Cc, Cs-corrected Sub-Ångström Low Voltage Electron Microscope (SALVE) at 30 - 80 kV. The EDX data were collected with a Talos F200X G2 STEM. ED data were collected with the FEI Titan TEM at 300 kV.

In order to extract the elemental composition from the EDX data, the peaks were fitted by spectra of selected elements, and the atomic fractions were calculated with the Brown-Powell model[75]. The energy resolution in the EELS experiments was determined to be 0.6 eV from the full width at half maximum of the zero-loss peak, measured in vacuum. If not stated otherwise in the corresponding spectra, for all presented core-loss EELS signals, the background was treated with a power-law model[76], which has shown to give good results in the previous studies of the analyzed elemental core-loss edges[77–79]. The thicknesses of the emerging annealed crystals were obtained from EELS by the log-ratio method[80,81].

For annealing experiments, a side entry Double Tilt Heating Holder Model 652-Ta (Gatan Inc.) and a FEI NanoEx-i/v - TEM holder was used (www.fei.com/nanoex). The transition temperature for the annealing experiments was measured directly from the FEI TEM holder at vacuum conditions ($7x10^{-9}$ bar). Here, the temperature was ramped to 250°C and then increased stepwise by ~ 10°C until phase

transformation occurred, and in a second step, the temperature was ramped to 900°C by ~ 50°C. For the structural investigation, the Model 652-Ta was used, and the sample was heated to 600°C for 40 min in vacuum ($1x10^{-5}$ bar) and analyzed subsequently at room temperature.

3D ED data were processed with *EDT-collect* program (Analitex, Stockholm, Sweden), supported by self-written MatLab scripts.

All HRTEM image calculations for the different observed $MnS_{1-x}P_x$ phases were performed using the open source *abTEM* Python Application Programming Interface (API), which is based on the multislice algorithm[82]. Experimentally determined image parameters were used as input parameters, and noise following the Poisson statistics[83] was added to the images to account for the finite electron dose. For all image calculations a stoichiometry of $MnS_{0.95}P_{0.05}$ was assumed.

All FFT-mask filtered images were generated following the numerical filtering protocol used for identifying grains in $MoSe_2$[84].

Computational methods: The energetics and electronic structure of all point defects were investigated using spin-polarized density functional theory (DFT) as implemented in VASP code[85,86]. All the calculations were carried out using PBE exchange-correlation functional[87]. For electronic structure calculations, the DFT + U method with an effective Hubbard value (U) of 5.5 eV for Mn atoms was employed. HSE06 calculations were carried out using the Heyd-Scuseria-Ernzerhof (HSE) hybrid functional[88,89].

The stability analysis for MnS_xP_{1-x} has been carried out by starting from fully relaxed MnS phase 4x4x2 supercell with plane wave cut-off 400 eV and 2x2x1 k-points according to Monkhorst-Pack scheme. The force convergence is set to 0.01 eV/ Å. Then S atoms are subsequently randomly substituted by P atoms until MnP structure is formed. The formation enthalpy has been evaluated with isolated atoms as the reference configuration. Additionally, the configurational entropy is considered, where S_{conf} = kB ln(W) and W is the number of different configurations for a given compound, evaluated using the binomial coefficient n over k, with n being the total number of available sites and k the number of impurities (for $Mn_{32}P_7S_{25}$, n=32, k=7).

Acknowledgment

We want to thank all cooperation associates in the framework of this manuscript. Further, we especially thank the Institut Laue-Langevin for the synthesis of the TMPT materials used in this work. This work was supported by the German Science Foundation (DFG), project CRC 1279 (project number 316249678), projects KR 4866/8-1, and the collaborative research center “Chemistry of Synthetic 2D Materials” SFB-1415-417590517. This work is supported by a project funded by Carl Zeiss foundation.

We acknowledge funding from the European Union's Horizon 2020 research and innovation programme under Grant Agreement No. 881603 (GrapheneCore3). The computational support from the Technical University of Dresden computing cluster (TAURUS) and High-Performance Computing Center (HLRS) in Stuttgart is gratefully appreciated. M.K.K acknowledges funding from the Deutsche Forschungsgemeinschaft (DFG) within the project DFG: KI 2546/1-1.

Supporting Information Available

HRTEM image series of $MnPS_3$ with corresponding FFTs and FFT-mask filtered images. STEM image series and corresponding elemental quantifications of $MnPS_3$ irradiated with a constant electron dose. Additional 3D ED data of irradiated $MnPS_3$. Spatially resolved EELS of the observed new phase. HRTEM image of an irradiated $MnPS_3$ flake showing the different orientations of the observed new phases. Formation enthalpy and convex hull calculations of $MnS_{1-x}P_x$ crystals as a function P concentration. TEM overview image series of the phase transformation process at an annealing temperature of 490°C. Elemental Maps, SAED, and additional core-loss EELS data of an annealed sample position annealed at 600°C. Further HRTEM, elemental maps, and quantifications of a $MnPS_3$ sample annealed at 900°C. Magnetic ordering and electronic band structure for different orientations of MnS slabs.

References

(1) Watanabe, T. Grain Boundary Engineering: Historical Perspective and Future Prospects. *J. Mater. Sci.* **2011**, *46* (12), 4095–4115.

(2) Zubko, P.; Gariglio, S.; Gabay, M.; Ghosez, P.; Triscone, J. M. Interface Physics in Complex Oxide Heterostructures. *Annu. Rev. Condens. Matter Phys.* **2011**, *2* (1), 141–165.

(3) Wang, L.; Xu, Z.; Wang, W.; Bai, X. Atomic Mechanism of Dynamic Electrochemical Lithiation Processes of MoS_2 Nanosheets. *J. Am. Chem. Soc.* **2014**, *136* (18), 6693–6697.

(4) Kühne, M.; Börrnert, F.; Fecher, S.; Ghorbani-Asl, M.; Biskupek, J.; Samuelis, D.; Krasheninnikov, A. V.; Kaiser, U.; Smet, J. H. Reversible Superdense Ordering of Lithium between Two Graphene Sheets. *Nature* **2018**, *564* (7735), 234–239.

(5) Hong, J.; Hu, Z.; Probert, M.; Li, K.; Lv, D.; Yang, X.; Gu, L.; Mao, N.; Feng, Q.; Xie, L.; Zhang, J.; Wu, D.; Zhang, Z.; Jin, C.; Ji, W.; Zhang, X.; Yuan, J.; Zhang, Z. Exploring Atomic Defects in Molybdenum Disulphide Monolayers. *Nat. Commun.* **2015**, *6* (1), 6293.

(6) Liu, C.; Malladi, S. K.; Xu, Q.; Chen, J.; Tichelaar, F. D.; Zhuge, X.; Zandbergen, H. W. In-Situ STEM Imaging of Growth and Phase Change of Individual $CuAl_X$ Precipitates in Al Alloy. *Sci. Rep.* **2017**, *7* (1), 3–10.

(7) Li, G.; Zhang, Y.-Y.; Guo, H.; Huang, L.; Lu, H.; Lin, X.; Wang, Y.-L.; Du, S.; Gao, H.-J. Epitaxial

Growth and Physical Properties of 2D Materials beyond Graphene: From Monatomic Materials to Binary Compounds. *Chem. Soc. Rev.* **2018**, *47* (16), 6073–6100.

(8) Huang, Y.; Pan, Y.-H.; Yang, R.; Bao, L.-H.; Meng, L.; Luo, H.-L.; Cai, Y.-Q.; Liu, G.-D.; Zhao, W.-J.; Zhou, Z.; Wu, L.-M.; Zhu, Z.-L.; Huang, M.; Liu, L.-W.; Liu, L.; Cheng, P.; Wu, K.-H.; Tian, S.-B.; Gu, C.-Z.; Shi, Y.-G.; Guo, Y.-F.; Cheng, Z. G.; Hu, J.-P.; Zhao, L.; Yang, G.-H.; Sutter, E.; Sutter, P.; Wang, Y.-L.; Ji, W.; Zhou, X.-J.; Gao, H.-J. Universal Mechanical Exfoliation of Large-Area 2D Crystals. *Nat. Commun.* **2020**, *11* (1), 2453.

(9) Komsa, H.-P.; Krasheninnikov, A. V. Effects of Confinement and Environment on the Electronic Structure and Exciton Binding Energy of MoS_2 from First Principles. *Phys. Rev. B* **2012**, *86* (24), 241201.

(10) Lehnert, T.; Lehtinen, O.; Algara-Siller, G.; Kaiser, U. Electron Radiation Damage Mechanisms in 2D $MoSe_2$. *Appl. Phys. Lett.* **2017**, *110* (3), 033106.

(11) Zhang, F.; Wang, Z.; Dong, J.; Nie, A.; Xiang, J.; Zhu, W.; Liu, Z.; Tao, C. Atomic-Scale Observation of Reversible Thermally Driven Phase Transformation in 2D In_2Se_3. *ACS Nano* **2019**, *13* (7), 8004–8011.

(12) Susi, T.; Meyer, J. C.; Kotakoski, J. Manipulating Low-Dimensional Materials down to the Level of Single Atoms with Electron Irradiation. *Ultramicroscopy* **2017**, *180*, 163–172.

(13) Susi, T.; Kotakoski, J.; Arenal, R.; Kurasch, S.; Jiang, H.; Skakalova, V.; Stephan, O.; Krasheninnikov, A. V.; Kauppinen, E. I.; Kaiser, U.; Meyer, J. C. Atomistic Description of Electron Beam Damage in Nitrogen-Doped Graphene and Single-Walled Carbon Nanotubes. *ACS Nano* **2013**, *7* (8), 7436.

(14) Meyer, J. C.; Eder, F.; Kurasch, S.; Skakalova, V.; Kotakoski, J.; Park, H. J.; Roth, S.; Chuvilin, A.; Eyhusen, S.; Benner, G.; Krasheninnikov, A. V.; Kaiser, U. Accurate Measurement of Electron Beam Induced Displacement Cross Sections for Single-Layer Graphene. *Phys. Rev. Lett.* **2012**, *108* (19), 196102.

(15) Susi, T.; Meyer, J. C.; Kotakoski, J. Quantifying Transmission Electron Microscopy Irradiation Effects Using Two-Dimensional Materials. *Nat. Rev. Phys.* **2019**, *1* (6), 397–405.

(16) Banhart, F.; Kotakoski, J.; Krasheninnikov, A. V. Structural Defects in Graphene. *ACS Nano* **2011**, *5* (1), 26–41.

(17) Zhou, W.; Zou, X.; Najmaei, S.; Liu, Z.; Shi, Y.; Kong, J.; Lou, J.; Ajayan, P. M.; Yakobson, B. I.; Idrobo, J. C. Intrinsic Structural Defects in Monolayer Molybdenum Disulfide. *Nano Lett.* **2013**, *13* (6), 2615–2622.

(18) Lin, Y. C.; Björkman, T.; Komsa, H. P.; Teng, P. Y.; Yeh, C. H.; Huang, F. S.; Lin, K. H.; Jadczak, J.; Huang, Y. S.; Chiu, P. W.; Krasheninnikov, A. V.; Suenaga, K. Three-Fold Rotational Defects in Two-Dimensional Transition Metal Dichalcogenides. *Nat. Commun.* **2015**, *6*, 6736.

(19) Komsa, H. P.; Kurasch, S.; Lehtinen, O.; Kaiser, U.; Krasheninnikov, A. V. From Point to Extended Defects in Two-Dimensional MoS_2: Evolution of Atomic Structure under Electron Irradiation. *Phys. Rev. B* **2013**, *88* (3), 035301.

(20) Wang, S.; Lee, G. Do; Lee, S.; Yoon, E.; Warner, J. H. Detailed Atomic Reconstruction of Extended Line Defects in Monolayer MoS_2. *ACS Nano* **2016**, *10* (5), 5419–5430.

(21) Lehnert, T.; Ghorbani-Asl, M.; Köster, J.; Lee, Z.; Krasheninnikov, A. V.; Kaiser, U. Electron-Beam-Driven Structure Evolution of Single-Layer $MoTe_2$ for Quantum Devices. *ACS Appl. Nano Mater.* **2019**, *2* (5), 3262–3270.

(22) Meyer, J. C.; Kurasch, S.; Park, H. J.; Skakalova, V.; Künzel, D.; Groß, A.; Chuvilin, A.; Algara-Siller, G.; Roth, S.; Iwasaki, T.; Starke, U.; Smet, J. H.; Kaiser, U. Experimental Analysis of Charge Redistribution Due to Chemical Bonding by High-Resolution Transmission Electron Microscopy. *Nat. Mater.* **2011**, *10* (3), 209–215.

(23) Susi, T.; Kotakoski, J.; Kepaptsoglou, D.; Mangler, C.; Lovejoy, T. C.; Krivanek, O. L.; Zan, R.; Bangert, U.; Ayala, P.; Meyer, J. C.; Ramasse, Q. Silicon-Carbon Bond Inversions Driven by 60-KeV Electrons in Graphene. *Phys. Rev. Lett.* **2014**, *113* (11), 115501.

(24) Lin, Y. C.; Dumcenco, D. O.; Huang, Y. S.; Suenaga, K. Atomic Mechanism of the Semiconducting-to-Metallic Phase Transition in Single-Layered MoS_2. *Nat. Nanotechnol.* **2014**, *9* (5), 391–396.

(25) Sutter, E.; Huang, Y.; Komsa, H. P.; Ghorbani-Asl, M.; Krasheninnikov, A. V.; Sutter, P. Electron-Beam Induced Transformations of Layered Tin Dichalcogenides. *Nano Lett.* **2016**, *16* (7), 4410–4416.

(26) Lin, Y.; Komsa, H.; Yeh, C.; Björkman, T.; Liang, Z.-Y.; Ho, C.-H.; Huang, Y.-S.; Chiu, P.-W.; Krasheninnikov, A. V.; Suenaga, K. Single-Layer ReS_2: Two-Dimensional Semiconductor with Tunable In-Plane Anisotropy. *ACS Nano* **2015**, *9* (11), 11249–11257.

(27) Chen, C. L.; Arakawa, K.; Lee, J. G.; Mori, H. Electron-Irradiation-Induced Phase Transformation in Alumina. *Scr. Mater.* **2010**, *63* (10), 1013–1016.

(28) Björkman, T.; Kurasch, S.; Lehtinen, O.; Kotakoski, J.; Yazyev, O. V.; Srivastava, A.; Skakalova, V.; Smet, J. H.; Kaiser, U.; Krasheninnikov, A. V. Defects in Bilayer Silica and Graphene: Common Trends in Diverse Hexagonal Two-Dimensional Systems. *Sci. Rep.* **2013**, *3*, 3482.

(29) Zhang, Z.; Liu, N.; Li, L.; Su, J.; Chen, P. P.; Lu, W.; Gao, Y.; Zou, J. In Situ TEM Observation of

Crystal Structure Transformation in InAs Nanowires on Atomic Scale. *Nano Lett.* **2018**, *18* (10), 6597–6603.

(30) Zhang, H.; Wang, W.; Xu, T.; Xu, F.; Sun, L. Phase Transformation at Controlled Locations in Nanowires by in Situ Electron Irradiation. *Nano Res.* **2020**, *13* (7), 1912–1919.

(31) Dang, Z.; Shamsi, J.; Palazon, F.; Imran, M.; Akkerman, Q. A.; Park, S.; Bertoni, G.; Prato, M.; Brescia, R.; Manna, L. In Situ Transmission Electron Microscopy Study of Electron Beam-Induced Transformations in Colloidal Cesium Lead Halide Perovskite Nanocrystals. *ACS Nano* **2017**, *11* (2), 2124–2132.

(32) Zhang, J.; Liu, J.; Huang, J. L.; Kim, P.; Lieber, C. M. Creation of Nanocrystals Through a Solid-Solid Phase Transition Induced by an STM Tip. *Science* **1996**, *274* (5288), 757–760.

(33) Mali, K. S.; Wu, D.; Feng, X.; Müllen, K.; Van der Auweraer, M.; De Feyter, S. Scanning Tunneling Microscopy-Induced Reversible Phase Transformation in the Two-Dimensional Crystal of a Positively Charged Discotic Polycyclic Aromatic Hydrocarbon. *J. Am. Chem. Soc.* **2011**, *133* (15), 5686–5688.

(34) Brown, B. E. The Crystal Structures of WTe_2 and High-Temperature $MoTe_2$. *Acta Crystallogr.* **1966**, *20* (2), 268–274.

(35) Cho, S.; Kim, S.; Kim, J. H.; Zhao, J.; Seok, J.; Keum, D. H.; Baik, J.; Choe, D.; Chang, K. J.; Suenaga, K.; Kim, S. W.; Lee, Y. H.; Yang, H. Phase Patterning for Ohmic Homojunction Contact in $MoTe_2$. *Science* **2015**, *349* (6248), 625–628.

(36) Duerloo, K. A. N.; Li, Y.; Reed, E. J. Structural Phase Transitions in Two-Dimensional Mo- and W-Dichalcogenide Monolayers. *Nat. Commun.* **2014**, *5*, 4214.

(37) Hou, W.; Azizimanesh, A.; Sewaket, A.; Peña, T.; Watson, C.; Liu, M.; Askari, H.; Wu, S. M. Strain-Based Room-Temperature Non-Volatile $MoTe_2$ Ferroelectric Phase Change Transistor. *Nat. Nanotechnol.* **2019**, *14* (7), 668–673.

(38) Meng, L.; Ma, Y.; Si, K.; Xu, S.; Wang, J.; Gong, Y. Recent Advances of Phase Engineering in Group VI Transition Metal Dichalcogenides. *Tungsten* **2019**, *1* (1), 46–58.

(39) Brec, R. Review on Structural and Chemical Properties of Transition Metal Phosphorous Trisulfides MPS_3. *Solid State Ionics* **1986**, *22* (1), 3–30.

(40) Li, X.; Cao, T.; Niu, Q.; Shi, J.; Feng, J. Coupling the Valley Degree of Freedom to Antiferromagnetic Order. *Proc. Natl. Acad. Sci. U. S. A.* **2013**, *110* (10), 3738–3742.

(41) Long, G.; Zhang, T.; Cai, X.; Hu, J.; Cho, C. W.; Xu, S.; Shen, J.; Wu, Z.; Han, T.; Lin, J.; Wang, J.; Cai, Y.; Lortz, R.; Mao, Z.; Wang, N. Isolation and Characterization of Few-Layer Manganese

Thiophosphite. *ACS Nano* **2017**, *11* (11), 11330–11336.

(42) Lee, S.; Choi, K. Y.; Lee, S.; Park, B. H.; Park, J. G. Tunneling Transport of Mono- and Few-Layers Magnetic van Der Waals $MnPS_3$. *APL Mater.* **2016**, *4* (8), 086108.

(43) Chittari, B. L.; Park, Y.; Lee, D.; Han, M.; Macdonald, A. H.; Hwang, E.; Jung, J. Electronic and Magnetic Properties of Single-Layer MPX_3 Metal Phosphorous Trichalcogenides. *Phys. Rev. B* **2016**, *94* (18), 184428.

(44) Hashemi, A.; Komsa, H. P.; Puska, M.; Krasheninnikov, A. V. Vibrational Properties of Metal Phosphorus Trichalcogenides from First-Principles Calculations. *J. Phys. Chem. C* **2017**, *121* (48), 27207–27217.

(45) Long, G.; Henck, H.; Gibertini, M.; Dumcenco, D.; Wang, Z.; Taniguchi, T.; Watanabe, K.; Giannini, E.; Morpurgo, A. F. Persistence of Magnetism in Atomically Thin $MnPS_3$ Crystals. *Nano Lett.* **2020**, *20* (4), 2452–2459.

(46) Du, K. Z.; Wang, X. Z.; Liu, Y.; Hu, P.; Utama, M. I. B.; Gan, C. K.; Xiong, Q.; Kloc, C. Weak Van Der Waals Stacking, Wide-Range Band Gap, and Raman Study on Ultrathin Layers of Metal Phosphorus Trichalcogenides. *ACS Nano* **2016**, *10* (2), 1738–1743.

(47) Kumar, R.; Jenjeti, R. N.; Austeria, M. P.; Sampath, S. Bulk and Few-Layer $MnPS_3$: A New Candidate for Field Effect Transistors and UV Photodetectors. *J. Mater. Chem. C* **2019**, *7* (2), 324–329.

(48) Gibertini, M.; Koperski, M.; Morpurgo, A. F.; Novoselov, K. S. Magnetic 2D Materials and Heterostructures. *Nat. Nanotechnol.* **2019**, *14* (5), 408–419.

(49) Fukami, S.; Lorenz, V. O.; Gomonay, O. Antiferromagnetic Spintronics. *J. Appl. Phys.* **2020**, *128* (7), 070401.

(50) Glass, D. E.; Jones, J.-P.; Shevade, A. V.; Bugga, R. V. Transition Metal Phosphorous Trisulfides as Cathode Materials in High Temperatures Batteries. *J. Electrochem. Soc.* **2020**, *167* (11), 110512.

(51) Wang, Y.; Zhou, Z.; Wen, T.; Zhou, Y.; Li, N.; Han, F.; Xiao, Y.; Chow, P.; Sun, J.; Pravica, M.; Cornelius, A. L.; Yang, W.; Zhao, Y. Pressure-Driven Cooperative Spin-Crossover, Large-Volume Collapse, and Semiconductor-to-Metal Transition in Manganese(II) Honeycomb Lattices. *J. Am. Chem. Soc.* **2016**, *138* (48), 15751–15757.

(52) Harms, N. C.; Kim, H. S.; Clune, A. J.; Smith, K. A.; O'Neal, K. R.; Haglund, A. V.; Mandrus, D. G.; Liu, Z.; Haule, K.; Vanderbilt, D.; Musfeldt, J. L. Piezochromism in the Magnetic Chalcogenide $MnPS_3$. *npj Quantum Mater.* **2020**, *5* (1), 56.

(53) Wang, Y.; Bai, L.; Wen, T.; Yang, L.; Gou, H.; Xiao, Y.; Chow, P.; Pravica, M.; Yang, W.; Zhao, Y. Giant Pressure-Driven Lattice Collapse Coupled with Intermetallic Bonding and Spin-State Transition in Manganese Chalcogenides. *Angew. Chemie - Int. Ed.* **2016**, *55* (35), 10350–10353.

(54) Clement, R.; Girerd, J. J.; Morgenstern-Badarau, I. Dramatic Modification of the Magnetic Properties of Lamellar Manganese Trithiophosphonite ($MnPS_3$) Upon Intercalation. *Inorg. Chem.* **1980**, *19* (9), 2852–2854.

(55) Coradin, T.; Coupé, A.; Livage, J. Intercalation of Biomolecules in the $MnPS_3$ Layered Phase. *J. Mater. Chem.* **2003**, *13* (4), 705–707.

(56) El-Meligi, A. A.; Al-Saie, A. M.; Al-Buflasa, H.; Bououdina, M. Formation of Composite Nanomaterial $MnPS_3$ Layered Structure Intercalated with Pyridine. *J. Alloys Compd.* **2009**, *488* (1), 284–290.

(57) Veerasubramani, G. K.; Park, M. S.; Choi, J. Y.; Lee, Y. S.; Kim, S. J.; Kim, D. W. Rational Combination of an Alabandite MnS Laminated Pyrrhotite $Fe_{1-x}S$ Nanocomposite as a Superior Anode Material for High Performance Sodium-Ion Battery. *ACS Sustain. Chem. Eng.* **2019**, *7* (6), 5921–5930.

(58) Li, S.; Chen, J.; Xiong, J.; Gong, X.; Ciou, J.; Lee, P. S. Encapsulation of MnS Nanocrystals into N, S-Co-Doped Carbon as Anode Material for Full Cell Sodium-Ion Capacitors. *Nano-Micro Lett.* **2020**, *12* (1), 34.

(59) Chen, X.; Li, W.; Xu, Y.; Zeng, Z.; Tian, H.; Velayutham, M.; Shi, W.; Li, W.; Wang, C.; Reed, D.; Khramtsov, V. V.; Li, X.; Liu, X. Charging Activation and Desulfurization of MnS Unlock the Active Sites and Electrochemical Reactivity for Zn-Ion Batteries. *Nano Energy* **2020**, *75*, 104869.

(60) Li, N.; Zhang, Y.; Cheng, R.; Wang, J.; Li, J.; Wang, Z.; Sendeku, M. G.; Huang, W.; Yao, Y.; Wen, Y.; He, J. Synthesis and Optoelectronic Applications of a Stable P-Type 2D Material: α-MnS. *ACS Nano* **2019**, *13* (11), 12662–12670.

(61) Köster, J.; Storm, A.; Ghorbani-Asl, M.; Kretschmer, S.; Gorelik, T. E.; Krasheninnikov, A. V.; Kaiser, U. Structural and Chemical Modifications of Few-Layer Transition Metal Phosphorous Trisulfides by Electron Irradiation. *J. Phys. Chem. C* **2022**, *126* (36), 15446–15455.

(62) Crozier, P. A.; McCartney, M. R.; Smith, D. J. Observation of Exit Surface Sputtering in TiO_2 Using Biased Secondary Electron Imaging. *Surf. Sci.* **1990**, *237* (1–3), 232–240.

(63) Medlin, D. L.; Howitt, D. G. The Role of Sputtering and Displacement Damage in the Electron SCRIBE Process. *Philos. Mag. Lett.* **1991**, *64* (3), 133–141.

(64) Egerton, R. F.; Li, P.; Malac, M. Radiation Damage in the TEM and SEM. *Micron* **2004**, *35* (6),

399–409.

(65) Komsa, H. P.; Kotakoski, J.; Kurasch, S.; Lehtinen, O.; Kaiser, U.; Krasheninnikov, A. V. Two-Dimensional Transition Metal Dichalcogenides under Electron Irradiation: Defect Production and Doping. *Phys. Rev. Lett.* **2012**, *109* (3), 035503.

(66) Yoshimura, A.; Lamparski, M.; Kharche, N.; Meunier, V. First-Principles Simulation of Local Response in Transition Metal Dichalcogenides under Electron Irradiation. *Nanoscale* **2018**, *10* (5), 2388–2397.

(67) Gemmi, M.; Mugnaioli, E.; Gorelik, T. E.; Kolb, U.; Palatinus, L.; Boullay, P.; Hovmöller, S.; Abrahams, J. P. 3D Electron Diffraction: The Nanocrystallography Revolution. *ACS Cent. Sci.* **2019**, *5* (8), 1315–1329.

(68) Clendenen, R. L.; Drickamer, H. G. Lattice Parameters of Nine Oxides and Sulfides as a Function of Pressure. *J. Chem. Phys.* **1966**, *44* (11), 4223–4228.

(69) Sombuthawee, C.; Bonsall, S. B.; Hummel, F. A. Phase Equilibria in the Systems ZnS-MnS, ZnS-$CuInS_2$, and MnS-$CuInS_2$. *J. Solid State Chem.* **1978**, *25* (4), 391–399.

(70) Prince, A. *Alloy Phase Equilibria*; Elsevier Publishing Co.: Amsterdam, 1966.

(71) Tan, H.; Verbeeck, J.; Abakumov, A.; Van Tendeloo, G. Oxidation State and Chemical Shift Investigation in Transition Metal Oxides by EELS. *Ultramicroscopy* **2012**, *116*, 24–33.

(72) Yang, Z.; Peng, H.; Sun, J.; Perdew, J. P. More Realistic Band Gaps from Meta-Generalized Gradient Approximations: Only in a Generalized Kohn-Sham Scheme. *Phys. Rev. B* **2016**, *93* (20), 205205.

(73) Blancá, E. L. P. y; Rodríguez, C. O.; Shitu, J.; Novikov, D. L. Degree of Localization of the Exchange-Correlation Hole and Its Influence on the Ground-State (Structural and Magnetic) Properties of d Metals. *J. Phys. Condens. Matter* **2001**, *13* (42), 9463–9470.

(74) Köster, J.; Liang, B.; Storm, A.; Kaiser, U. Polymer-Assisted TEM Specimen Preparation Method for Oxidation-Sensitive 2D Materials. *Nanotechnology* **2021**, *32* (7), 075704.

(75) Powell, C. J. Cross Sections for Ionization of Inner-Shell Electrons by Electrons. *Rev. Mod. Phys.* **1976**, *48* (1), 33–47.

(76) Egerton, R. F. *Electron Energy-Loss Spectroscopy in the Electron Microscope*, 3rd ed.; Springer New York Dordrecht Heidelberg London, 2011.

(77) Van Aken, P. A.; Liebscher, B.; Styrsa, V. J. Quantitative Determination of Iron Oxidation States in Minerals Using Fe $L_{2,3}$-Edge Electron Energy-Loss Near-Edge Structure Spectroscopy. *Phys.*

Chem. Miner. **1998**, *25*, 323–327.

(78) Van Aken, P. A.; Liebscher, B. Quantification of Ferrous/Ferric Ratios in Minerals: New Evaluation Schemes of Fe L_{23} Electron Energy-Loss Near-Edge Spectra. *Phys. Chem. Miner.* **2002**, *29* (3), 188–200.

(79) Tan, H.; Verbeeck, J.; Abakumov, A.; Tendeloo, G. Van. Ultramicroscopy Oxidation State and Chemical Shift Investigation in Transition Metal Oxides by EELS. *Ultramicroscopy* **2012**, *116*, 24–33.

(80) Malis, T.; Cheng, S. C.; Egerton, R. F. EELS Log-Ratio Technique for Specimen-Thickness Measurement in the TEM. *J. Electron Microsc. Tech.* **1988**, *8* (2), 193–200.

(81) Köster, J.; Storm, A.; Gorelik, T. E.; Mohn, M. J.; Port, F.; Gonçalves, M. R.; Kaiser, U. Evaluation of TEM Methods for Their Signature of the Number of Layers in Mono- and Few-Layer TMDs as Exemplified by MoS_2 and $MoTe_2$. *Micron* **2022**, *160*, 103303.

(82) Madsen, J.; Susi, T. The AbTEM Code: Transmission Electron Microscopy from First Principles. *Open Res. Eur.* **2021**, *1*, 24.

(83) De Graef, M. *Introduction to Conventional Transmission Electron Microscopy*; Cambridge University Press, 2003.

(84) Lehtinen, O.; Komsa, H. P.; Pulkin, A.; Whitwick, M. B.; Chen, M. W.; Lehnert, T.; Mohn, M. J.; Yazyev, O. V.; Kis, A.; Kaiser, U.; Krasheninnikov, A. V. Atomic Scale Microstructure and Properties of Se-Deficient Two-Dimensional $MoSe_2$. *ACS Nano* **2015**, *9* (3), 3274–3283.

(85) Kresse, G.; Furthmüller, J. Efficient Iterative Schemes for Ab Initio Total-Energy Calculations Using a Plane-Wave Basis Set. *Phys. Rev. B* **1996**, *54* (16), 11169–11186.

(86) Kresse, G.; Furthmüller, J. Efficiency of Ab-Initio Total Energy Calculations for Metals and Semiconductors Using a Plane-Wave Basis Set. *Comput. Mater. Sci.* **1996**, *6* (1), 15–50.

(87) Perdew, J. P.; Burke, K.; Ernzerhof, M. Generalized Gradient Approximation Made Simple. *Phys. Rev. Lett.* **1996**, *77* (18), 3865–3868.

(88) Heyd, J.; Scuseria, G. E.; Ernzerhof, M. Hybrid Functionals Based on a Screened Coulomb Potential. *J. Chem. Phys.* **2003**, *118* (18), 8207–8215.

(89) Paier, J.; Marsman, M.; Hummer, K.; Kresse, G.; Gerber, I. C.; Angyán, J. G. Screened Hybrid Density Functionals Applied to Solids. *J. Chem. Phys.* **2006**, *124* (15), 154709.
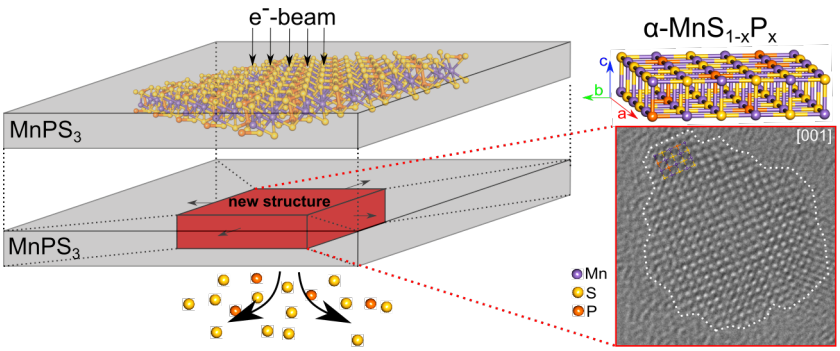
For Table of Contents Only